Formation of organized nanostructures from unstable bilayers of thin metallic liquids

Mikhail Khenner, Sagar Yadavali, and Ramki Kalyanaraman

Citation: Phys. Fluids **23**, 122105 (2011); doi: 10.1063/1.3665618
View online: http://dx.doi.org/10.1063/1.3665618
View Table of Contents: http://pof.aip.org/resource/1/PHFLE6/v23/i12
Published by the American Institute of Physics.

Formation of organized nanostructures from unstable bilayers of thin metallic liquids

Mikhail Khenner,[1,2] Sagar Yadavali,[3] and Ramki Kalyanaraman[3,4,5]
[1]*Department of Mathematics and Computer Science, Western Kentucky University, Bowling Green, Kentucky 42101, USA*
[2]*Applied Physics Institute, Western Kentucky University, Bowling Green, Kentucky 42101, USA*
[3]*Department of Chemical and Biomolecular Engineering, The University of Tennessee, Knoxville, Tennessee 37996, USA*
[4]*Department of Materials Science and Engineering, The University of Tennessee, Knoxville, Tennessee 37996, USA*
[5]*Sustainable Energy Education Research Center, The University of Tennessee, Knoxville, Tennessee 37996, USA*

(Received 15 April 2011; accepted 8 November 2011; published online 20 December 2011)

Dewetting of pulsed-laser irradiated, thin (<20 nm), optically reflective metallic bilayers on an optically transparent substrate with a reflective support layer is studied within the lubrication equations model. A steady-state bilayer film thickness (h) dependent temperature profile is derived based on the mean substrate temperature estimated from the elaborate thermal model of transient heating and melting/freezing. Large thermocapillary forces are observed along the plane of the liquid-liquid and liquid-gas interfaces due to this h-dependent temperature, which, in turn, is strongly influenced by the h-dependent laser light reflection and absorption. Consequently the dewetting is a result of the competition between thermocapillary and intermolecular forces. A linear analysis of the dewetting length scales established that the non-isothermal calculations better predict the experimental results as compared to the isothermal case within the bounding Hamaker coefficients. Subsequently, a computational non-linear dynamics study of the dewetting pathway was performed for Ag/Co and Co/Ag bilayer systems to predict the morphology evolution. We found that the systems evolve towards formation of different morphologies, including core-shell, embedded, or stacked nanostructure morphologies. © *2011 American Institute of Physics*. [doi:10.1063/1.3665618]

I. INTRODUCTION

Nanostructured surfaces and nanomaterials, such as nanoparticles that show multiple useful physical characteristics (for instance, magnetism and plasmonics), could be very useful towards sensing and detection, including of surface chemical interactions. As a result, advances will be to applications in biocatalysis,[1–3] biosensing,[4] high-density magneto-optical technologies,[5] and semiconductor computing and switching utilizing spintronic effects.[6] Such a surface can be envisioned to be made from nanostructures of different metals, such as of Ag (which is plasmon active) and Co (which is ferromagnetic), in which the morphology characteristics (for instance, core-shell or composite structures), will determine the physical response.[7,8] Therefore, control of the nanoscale features, especially at length scales below the diffraction limit of light, is an ongoing challenge.

There are limited techniques, such as lithography,[9] solution processing,[10] and self-organization,[11] that have demonstrated the synthesis of such multi-component nanomaterials. Spontaneous self-organizing processes that lead to nanostructure formation are often attractive because of the intrinsic robustness and low cost. One such process that is being harnessed to create complex nanostructures is the spontaneous spinodal dewetting of thin polymeric liquid films from its contact surface.[12–14] For an ultrathin film on a non-wetting substrate, long-range intermolecular attractive dispersion forces between the film and substrate, with magnitude determined by the Hamaker coefficient A, lead to an unstable thermodynamic free energy which can have a spinodal character, i.e., the free energy curvature <0. Consequently, for such thin films, a height perturbation of the liquid film surface, such as by capillary waves, can result in a free energy decrease, leading to spontaneous spinodal dewetting.[12,13] In order to observe this behavior in metals, which have extremely high melting temperatures, practical ways to access the liquid phase are necessary. Therefore, studies of pattern formation in metal films have focused on the use of ion irradiation[15,16] or pulsed laser irradiation.[17–19]

Laser-irradiation of metallic films exhibit a variety of spatio-temporal instabilities leading to formation of different nanomorphologies.[20–23] The present paper is motivated by the recent experiments on dewetting of non-reactive, immiscible metallic bilayers done in our group,[11] and the need to better understand the physical mechanisms leading to spatial ordering of particles, and the morphological pathways towards the final particle morphologies. The experimental[24–31] and theoretical[32–41] studies of the instabilities and dynamics of bilayer thin films so far have been largely limited to aqueous and polymer systems under isothermal conditions. Non-isothermal dewetting even in such more conventional systems has not been fully investigated theoretically. Indeed, in Refs. 32 and 33, the equation set that accounts for the Marangoni effect is derived, but only the analysis and some computations in the isothermal case

are performed; and in Refs. 39–41, either a special set of Hamaker coefficients is considered, such that dewetting exhibits autophobic behavior, or in addition a longitudinal temperature gradient is considered.

Pulsed laser irradiation of single-layer metal thin films has been shown to introduce thermocapillary effects along the film–ambient surface and thus influence the pattern formation in single layer films.[22,42,43] The primary reason for the appearance of the thermocapillary effect is a non-trivial (i.e., non-linear) dependence of the temperature on film thickness, which is due to the thickness-dependent laser light reflectivity and absorption.[22,42] In this work, for the first time, we show that similar thermocapillary effects appear in bilayer films irradiated by the laser. As a consequence, it is important to study the non-isothermal dewetting instability in order to better predict future experimental investigations of the morphology evolution. Therefore, in this work, we explore theoretically and computationally the isothermal as well as non-isothermal instabilities and morphological evolution in laser-melted bilayers. The paper is divided into major sections as follows. In Sec. II, we detail the bilayer evolution equations and the thermal problem. The systems under consideration are metallic bilayers (of Ag/Co and Co/Ag) in contact with a transparent SiO_2 substrate formed on a reflective Si support layer. We evaluated the steady state bilayer film temperature profile by utilizing the mean substrate temperature estimated from an elaborate thermal model of transient heating and melting/freezing. In Sec. III, linear stability analysis was performed to obtain the dewetting instability length scales for the isothermal as well as non-isothermal cases. These results were compared to experimental measurements of length scales for the Ag/Co and Co/Ag bilayers presented in Ref. 11. Previously, we found, using an energy rate analysis approach, that the experimental results could be bounded by theory predictions provided two sets of Hamaker coefficients were used. This was a consequence of the uncertainity in the Hamaker coefficient values and the different techniques used to calculate them. Here, we followed a similar approach in the linear analysis. We found that the non-isothermal results were a better match to the experimental results as compared to the isothermal case. Consequently, this motivated us to pursue the full non-linear evolution dynamics in the non-isothermal as well as isothermal cases. This work is presented in Sec. IV. The calculations were performed for the Ag/Co and Co/Ag systems as a function of the upper layer thickness. We found differences in the morphological characteristics, including core-shell, embedded, or stacked nanostructure morphologies. In addition, we also found that for certain cases, the non-isothermal evolution predicts different morphologies from the isothermal case. These results are likely to be very useful towards guiding future experiments that investigate the correlation between morphology and physical characteristics.

II. PROBLEM STATEMENT

A. Evolution equations for the bilayer

We consider a bilayer thin film, which is comprised of two superposed layers of immiscible Newtonian liquids, for instance, the molten Co and Ag; see Fig. 1. The lower layer rests on a solid, planar substrate (denoted by the subscript s hereafter) that has thickness h_s and the upper layer is in contact with the adjacent gas phase. The locations of the liquid-liquid and the liquid-gas interfaces are given by $z = h_1(x,t)$ and $z = h_2(x,t)$, respectively, where z,x are the vertical and the horizontal coordinates, respectively, with $z = 0$ corresponding to the location of substrate/liquid interface. The bilayer is irradiated by a single pulsed laser beam, such that the pulse width typically is 10 ns and the frequency of pulses is 50 Hz.

In the case of a single-layer film, dewetting has been successfully modeled as continuous in time by treating the film as liquid despite that it re-solidifies after each pulse. Thermocapillary effect owing to latent heat release is negligible due to extremely large cooling rates involved;[19] the film cools down so fast that there is insufficient time for any morphology change,[44] and the next incident laser pulse effectively quenches in the film. The time and length scales involved and the resulting morphologies are captured very well by such models.[19,22,43]

In this paper, we adopt the same strategy for the bilayer film modeling. Hereafter, a two-dimensional geometry is

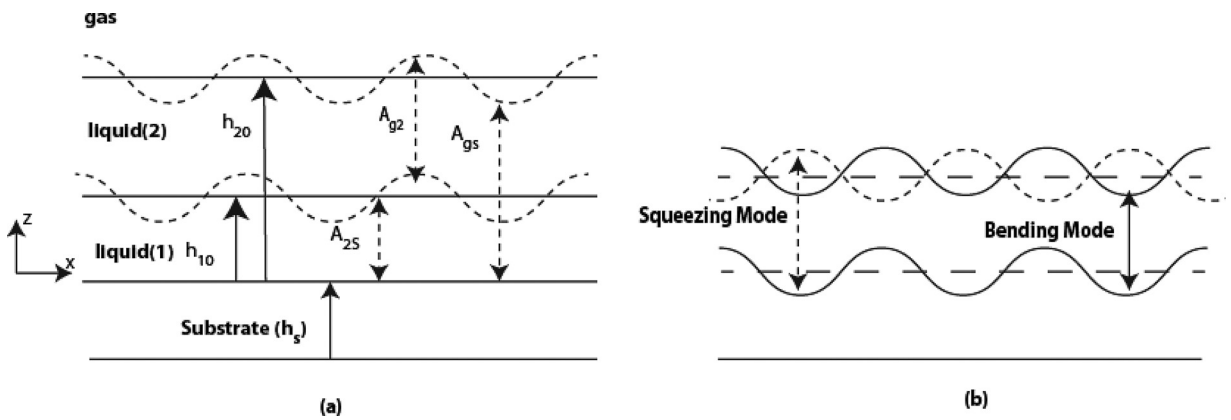

FIG. 1. (a) Liquid bilayer/substrate system. Here A_{g2}, A_{gs}, and A_{2s} are Hamaker coefficients of the intermolecular repulsion or attraction force, h_{10}, h_{20} are the unperturbed thicknesses of the liquid layers, and h_s is the thickness of SiO_2 substrate. Si support layer is not shown. (b) Deformation modes of the two interfaces.

considered; thus we assume that liquid flow is negligible in the transverse direction.

The derivation of the evolution equations for the functions $h_{1,2}(x,t)$, describing the shapes of the two interfaces, is detailed in Ref. 34 in the isothermal case and in Refs. 33, 39, and 40 in the more general non-isothermal case characterized by the presence of thermocapillary (Marangoni) forces. (Hereafter, the notation $f_{\alpha,\beta}$ means f_α, f_β.) These derivations assume that the characteristic spatial scale in the x-direction is much larger than in the z-direction (layers are thin), so that the fluid flow in the layers is described by Stokes equations. The derivation procedure is routinely called the long-wave (or lubrication) approximation. A thorough discussions of the long-wave approach to the studies of the instabilities of thin liquid films can be found in the review papers.[45–47]

Here, we start with the non-isothermal system of equations, where the thermocapillary effect is accounted for at the liquid-liquid and liquid-gas interfaces[32,33,39,40]

$$\partial_t h_1 = -\partial_x[F_{11}\partial_x P_1 + F_{12}\partial_x P_2 + \Phi_{11}\partial_x\sigma_1 + \Phi_{12}\partial_x\sigma_2], \quad (1)$$

$$\partial_t h_2 = -\partial_x[F_{21}\partial_x P_1 + F_{22}\partial_x P_2 + \Phi_{21}\partial_x\sigma_1 + \Phi_{22}\partial_x\sigma_2], \quad (2)$$

where $P_{1,2}$ are the pressures and $\sigma_{1,2}$ are the surface tensions of the liquid-liquid and liquid-gas interface, respectively. The quantities F_{ij} and Φ_{ij}, $i,j=1,..,2$ are given by

$$F_{11} = -\frac{1}{3\eta_1}h_1^3, \quad F_{12} = -\frac{1}{2\eta_1}h_1^2\left(h_2 - \frac{h_1}{3}\right), \quad (3)$$

$$F_{21} = \frac{1}{6\eta_1}h_1^3 - \frac{1}{2\eta_1}h_1^2 h_2,$$
$$F_{22} = \frac{1}{3}(h_2-h_1)^3\left(\frac{1}{\eta_1}-\frac{1}{\eta_2}\right) - \frac{1}{3\eta_1}h_2^3, \quad (4)$$

$$\Phi_{11} = \Phi_{12} = \frac{1}{2\eta_1}h_1^2, \Phi_{21} = -\frac{1}{2\eta_1}h_1(h_1-2h_2), \quad (5)$$

$$\Phi_{22} = \frac{1}{2\eta_2}(h_2-h_1)^2 + \Phi_{21}, \quad (6)$$

where $\eta_{1,2}$ are the dynamic viscosities. The pressures are

$$P_1 = -\sigma_1\partial_{xx}h_1 - \sigma_2\partial_{xx}h_2 + \Pi_1(h_1,h_2) + \rho_1 g h_1 + \rho_2 g(h_2-h_1), \quad (7)$$

$$P_2 = -\sigma_2\partial_{xx}h_2 + \Pi_2(h_1,h_2) + \rho_2 g h_2, \quad (8)$$

where $\rho_{1,2}$ are the densities, g is the acceleration of gravity, and $\Pi_{1,2}(h_1,h_2)$ are the disjoining pressures, given by

$$\Pi_1(h_1,h_2) = \frac{A_{2s}}{h_1^3} + \frac{A_{gs}}{h_2^3} + \frac{S_1\exp\left(-\frac{h_1}{\ell_1}\right)}{l_1}, \quad (9)$$

$$\Pi_2(h_1,h_2) = \frac{A_{g2}}{(h_2-h_1)^3} + \frac{A_{gs}}{h_2^3} + \frac{S_2\exp\left(-\frac{(h_2-h_1)}{\ell_2}\right)}{l_2}. \quad (10)$$

Here, A_{g2}, A_{gs}, A_{2s} are the Hamaker coefficients describing the *long-range molecular repulsion or attraction*, depending on the sign of a coefficient (see Tables II and III), between the liquid-liquid and liquid-gas interface, solid-liquid and liquid-gas interface, and solid-liquid and liquid-liquid interface, respectively. $S_{1,2}<0$ are the spreading coefficients, describing the *short-range molecular repulsion* between the solid-liquid and liquid-liquid interface and liquid-liquid and liquid-gas interface, respectively. $\ell_{1,2}$ are the equilibrium cut-off distances. The short-range repulsion between the solid-liquid and liquid-gas interface is not included. Note that we include gravity terms in the pressures, since it has been shown that these terms may be important in a certain range of parameters.[35,41]

The surface tension gradients, $\partial_x\sigma_1$ and $\partial_x\sigma_2$, are caused by the gradients of the temperature at the liquid-liquid and the liquid-gas interface, respectively. We assume linear dependence of the surface tensions on temperature

$$\sigma_1 = \sigma_1^{(m)} - \gamma_1\left(T_1(z=h_1) - T_1^{(m)}\right), \quad \gamma_1 > 0, T_1(z=h_1) > T_1^{(m)}, \quad (11)$$

$$\sigma_2 = \sigma_2^{(m)} - \gamma_2\left(T_2(z=h_2) - T_2^{(m)}\right), \quad \gamma_2 > 0, T_2(z=h_2) > T_2^{(m)}, \quad (12)$$

where $\sigma_{1,2}^{(m)}$ are the surface tensions at the corresponding melting temperatures $T_{1,2}^{(m)}$. Since the temperatures $T_{1,2}$ will be shown to depend on the thicknesses of the layers, the surface tension gradients in Eqs. (1) and (2) are written as

TABLE I. The physical parameters.

Ag/Co/SiO_2/Si system	Co/Ag/SiO_2/Si system
$\eta_1 = 4.46\times10^{-3}$ Pa-s	$\eta_1 = 3.88\times10^{-3}$ Pa-s
$\eta_2 = 3.88\times10^{-3}$ Pa-s	$\eta_2 = 4.46\times10^{-3}$ Pa-s
$\sigma_1^{(m)} = 0.168$J/m^2	$\sigma_1^{(m)} = 0.168$J/m^2
$\sigma_2^{(m)} = 0.925$J/m^2	$\sigma_2^{(m)} = 1.88$J/m^2
$\gamma_1=\gamma_2 = 5\times10^{-5}$ J/(K m^2)	$\gamma_1=\gamma_2 = 5\times10^{-5}$ J/(K m^2)
$\rho_1 = 7.75\times10^3$ Kg/m^3	$\rho_1 = 9.32\times10^3$ Kg/m^3
$\rho_2 = 9.32\times10^3$ Kg/m^3	$\rho_2 = 7.75\times10^3$ Kg/m^3
$T_1^{(m)} = 1768$K	$T_1^{(m)} = 1235$K
$T_2^{(m)} = 1235$K	$T_2^{(m)} = 1768$K
$\Theta_a = 300$ K	$\Theta_a = 300$ K
$\Theta_s = 1850$ K	$\Theta_s = 1850$ K
$\delta_1=\delta_2 = 10^6$ m^{-1}	$\delta_1=\delta_2 = 10^6$ m^{-1}
$\alpha = 10^3$ W/(K m^2)	$\alpha = 10^3$ W/(K m^2)
$\kappa_1 = 34$ W/(K m)	$\kappa_1 = 185$ W/(K m)
$\kappa_2 = 185$ W/(K m)	$\kappa_2 = 34$ W/(K m)
$\kappa_s = 50$ W/(K m)	$\kappa_s = 50$ W/(K m)
$h_s = 400$ nm	$h_s = 400$ nm
$J = 1.25\times10^{11}$ J/(s m^2)	$J = 1.25\times10^{11}$ J/(s m^2)

TABLE II. Hamaker coefficients for the Ag/Co/SiO_2/Si system.

Hamaker const.	Set I	Set II
A_{g2}	-10^{-20} J	-10^{-19} J
A_{gs}	4×10^{-20} J	4×10^{-20} J
A_{2s}	4×10^{-21} J	2×10^{-20} J

TABLE III. Hamaker coefficients for the Co/Ag/SiO_2/Si system.

Hamaker const.	Set I	Set II
A_{g2}	10^{-20} J	10^{-21} J
A_{gs}	10^{-20} J	10^{-18} J
A_{2s}	-10^{-22} J	-10^{-22} J

$$\partial_x \sigma_1 = -\gamma_1\left((\partial_{h_1} T_1)|_{z=h_1}\partial_x h_1 + (\partial_{h_2} T_1)|_{z=h_1}\partial_x h_2\right), \quad (13)$$

$$\partial_x \sigma_2 = -\gamma_2\left((\partial_{h_1} T_2)|_{z=h_2}\partial_x h_1 + (\partial_{h_2} T_2)|_{z=h_2}\partial_x h_2\right). \quad (14)$$

In order to close the equation set, we need the specification of the thermal problem. This is discussed in Sec. II B.

B. Thermal problem

The steady-state, long-wave energy equations in the two metallic layers and in the thin, purely conductive substrate are[19,43]

$$\frac{\kappa_{1,2}}{\rho_{1,2}C_{eff}}\partial_{zz}T_{1,2} + \frac{\delta_2 J}{\rho_{1,2}C_{eff}}(1 - R(h_1, h_2 - h_1))\exp\left(\delta_{1,2}(z - h_2)\right) = 0, \quad (15)$$

$$\frac{\kappa_s}{\rho_s C_{eff}}\partial_{zz}T_s = 0, \quad (16)$$

where $\kappa_{1,2,s}$ are the thermal conductivities, C_{eff} is the effective heat capacity, $\delta_{1,2}$ are the optical absorption coefficients, $\delta_2 J$ is the rate of the laser energy flux volumetric absorption into the upper layer, ρ_s is the substrate density, and $R(h_1, h_2 - h_1)$ is the dimensionless effective reflectivity function, which has been calculated using the method described in detail in Ref. 48 and 51. Equation (15) is the Beer-Lambert law for the bilayer.

Fig. 2(a) shows the contour plot of the reflectivity for Ag/Co/SiO_2/Si system. It can be seen that the reflectivity is shaped, roughly, like a Taco shell with the axis that makes the 120° angle to the horizontal axis in the plot. The plot for Co/Ag/SiO_2/Si system is similar. Fig. 2(b) shows the reflectivity of the Ag/Co/SiO_2/Si and Co/Ag/SiO_2/Si as a function of a varying thickness of the top film, with the thickness of the bottom film fixed at 1 nm. The thickness of the SiO_2 substrate is taken as 400 nm, consistent with the experimental system[11] to which we will compare our calculations. The non-monotonic dependence of the reflectivity on thickness is clearly evident from either plot, as is the increase of reflectivity as the thickness of the top film approaches zero. This is the result of increased reflectivity from the underlying reflective Si layer. This thickness dependent absorption (Eq. (15)) and reflectivity are responsible for the strong dependence of the thermocapillary forces on the thicknesses $h_{1,2}$.

The long-wave boundary conditions for the set of Eqs. (15) and (16) are

$$z = h_2: \quad \kappa_2 \partial_z T_2 = -\alpha(T_2 - \Theta_a), \quad (17)$$

$$z = h_1: \quad \kappa_1 \partial_z T_1 = \kappa_2 \partial_z T_2, T_1 = T_2, \quad (18)$$

$$z = 0: \quad \kappa_1 \partial_z T_1 = \kappa_s \partial_z T_s, T_1 = T_s, \quad (19)$$

$$z = -h_s: \quad T_s = \Theta_s, \quad (20)$$

where Θ_a and Θ_s are the (constant) gas and substrate temperatures, respectively, and α is the heat transfer coefficient at the liquid-gas interface.

The solution of this boundary-value problem in the liquid layers has the form

$$T_1 = -\frac{\delta_2 J(1 - R(h_1, h_2 - h_1))}{\delta_1^2 \kappa_1}\exp(\delta_1(z - h_2)) + c_{11}z + c_{12}, \quad (21)$$

$$T_2 = -\frac{J(1 - R(h_1, h_2 - h_1))}{\delta_2 \kappa_2}\exp(\delta_2(z - h_2)) + c_{21}z + c_{22}, \quad (22)$$

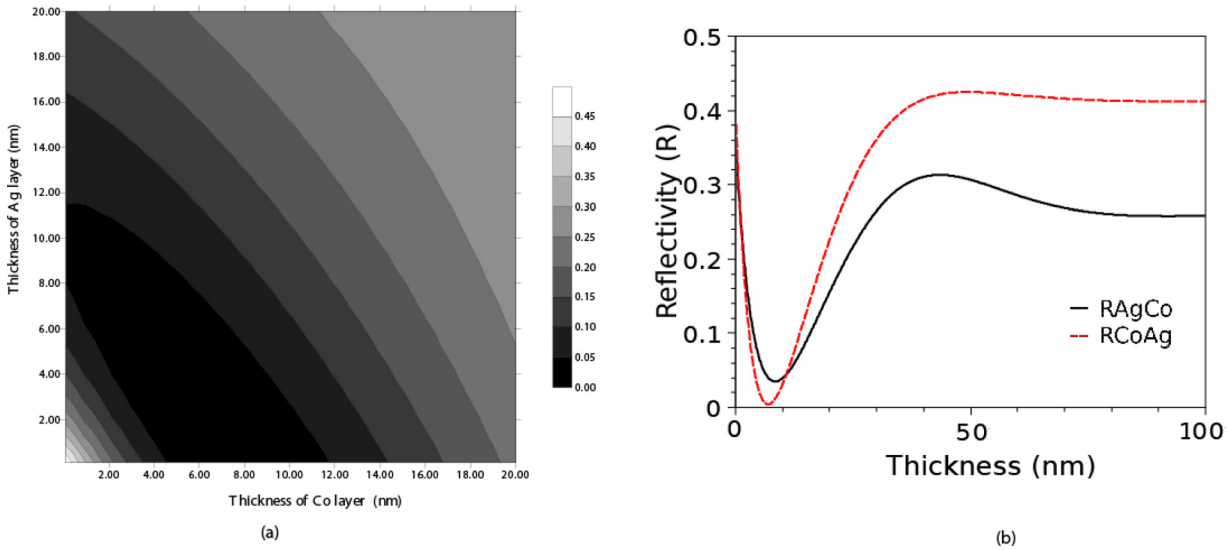

FIG. 2. (Color online) (a) Contour plot of the reflectivity for Ag/Co/SiO_2/Si system. The increased reflectivity when approaching zero top film thickness is due to the reflective underlying Si layer. (b) Reflectivity R of the bilayer metallic systems Ag/Co/SiO_2/Si and Co/Ag/SiO_2/Si as a function of a varying thickness of the top film; thickness of the bottom film is 1 nm.

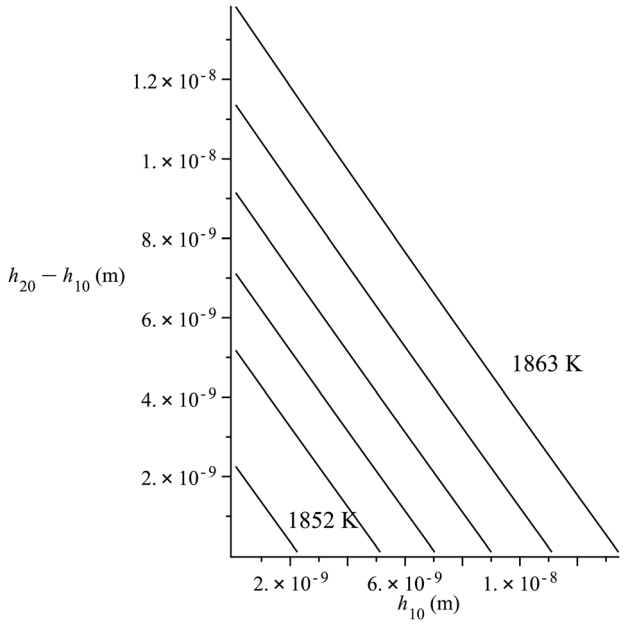

FIG. 3. Typical contour plot of the interface temperature as a function of h_1 and h_2.

where c_{ij} are the complicated functions of $h_{1,2,s}$,$\kappa_{1,2,s}$,$\delta_{1,2}$, J,α,Θ_a,Θ_s, which we obtained using the computer algebra system (CAS) (Mathematica). (In the substrate, the temperature is an increasing linear function of z, as is evident from Eq. (16). Note that the temperature profile in the bilayer (Eqs. (21) and (22)) is nonlinear in z. In the absence of the thickness-dependent reflectivity and absorption, the interfacial temperature gradients $\partial_{h_i} T_j$ in Eqs. (13) and (14) are constants rather than functions of $h_{1,2}$ (since in this case the temperature profile is linear in z with constant coefficients, as is encountered in films heated from the substrate[40]).

In the above presented formulation, the heat conduction in the thick Si support layer is disregarded, and the temperature at the SiO_2/Si interface is set equal to the mean substrate temperature Θ_s, estimated from the transient heating model for periods when the system is in the liquid state and for the typical values of the laser energy and the bilayer film thickness employed in this study (see Appendix). Θ_s is obtained by averaging over many pulses the temperature rise and fall within the width of the Gaussian pulse. Practically, this formulation also makes feasible the numerical evaluation, at every step of interfaces evolution, of the complicated analytical solution formulas for the steady-state temperatures of the metal layers and for the derivatives of these temperatures with respect to thicknesses h_1 and h_2. Note also, that even without accounting for the heat conduction in the support layer, this layer still exerts the important influence on the system's steady-state temperature field, since the effective reflectivity R is calculated for the full system metal$_1$/metal$_2$/SiO_2/Si.

Ignoring the transient nature of heat conduction due to intermittency of pulses is justified if the thermal diffusion time scale τ_H is much shorter than the dewetting time scale, τ_D. In our previous works,[19,22,42] on single-layer films we have shown that $\tau_H \sim h^4$, and $\tau_D \sim h^5$. Thus for sufficiently thick films $\tau_H < \tau_D$. In the bilayer system we expect similar general trend.

Fig. 3 shows the contour plot of either interface temperature, $T_1(z = h_{10})$ or $T_2(z = h_{20})$ (the plotting software cannot resolve the small difference (of the order of 1 K) of the interfacial temperatures). It can be seen that the temperature difference between the liquid/gas interface and the SiO_2/Si interface is small (of the order of 15 K or less). This parallels the results of the analysis of the model of transient heating, see Appendix and Ref. 19.

Next, we show that despite the typical temperature difference being small, the contributions from the thermocapillary surface tension gradient terms in the evolution Eqs. (1) and (2) are significant. Indeed, for Ag/Co/SiO_2/Si system, Fig. 4 shows the comparison of the linearized terms at the

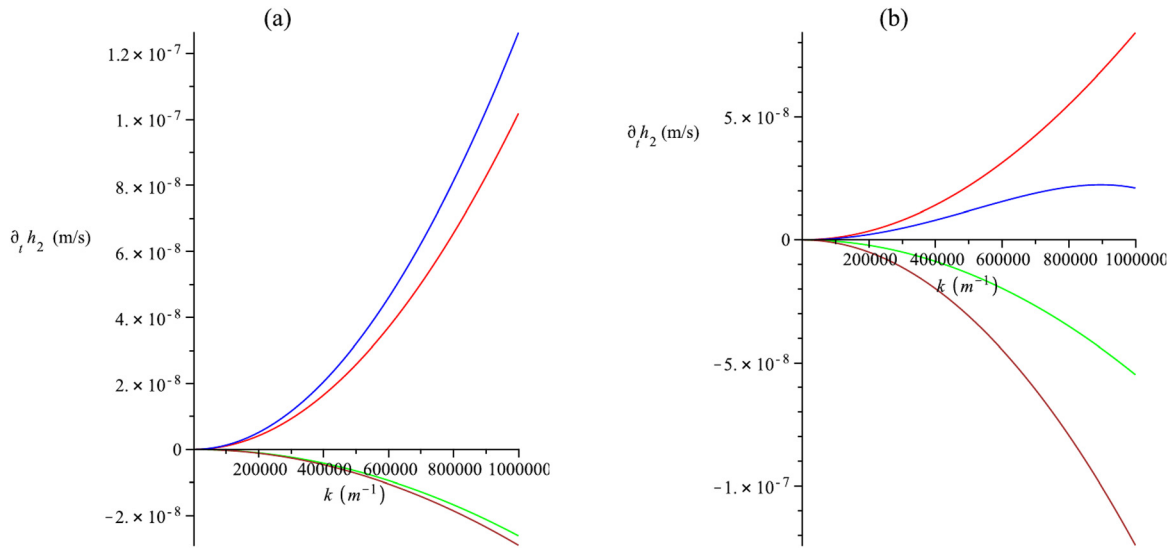

FIG. 4. (Color online). The linearized terms at the RHS of Eq. (2) at the interfacial deformations with the amplitude 0.1 nm from the mean values (a) $h_{10} = 5$ nm, $h_{20} = 7$ nm, (b) $h_{10} = 5$ nm, $h_{20} = 17$ nm. Red line: 1st term; blue line: 2nd term; green line: 3rd term; brown line: 4th term. Values along the vertical axis show the contribution of each term to the total velocity of the interface, not the total velocity itself.

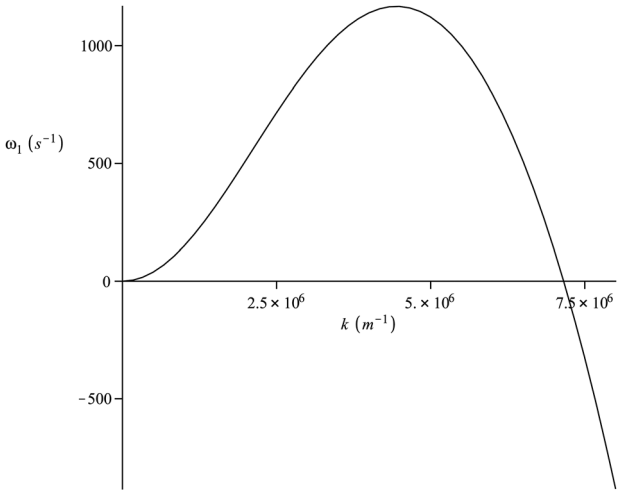

FIG. 5. Typical positive dispersion curve for the Ag/Co/SiO_2/Si system.

RHS of the evolution Eq. (2). These terms are calculated at the amplitudes of the interfaces deformations that are set equal to 0.1 nm, the values that are within reach of the linear approximation. (Deformation = amplitude × coskx, see Sec. III for more details on the linear stability analysis.) It can be seen that for thin films–that are the sole focus of this paper–the thermocapillary surface tension gradient terms 3 and 4 are negative and thus stabilizing, and their magnitudes are of the same order as the magnitudes of the pressure gradient terms 1 and 2. Same can be said of the terms at the RHS of the first evolution Eq. (1). Terms 3 and 4 are also negative for the parameters of the Co/Ag/SiO_2/Si system. For thick films ($h_{20} > 32$ nm for Ag/Co), these terms become positive and thus destabilizing. Thus, the situation here is similar to the case of a single-layer film; in Ref. 19, it is shown that Co films on the SiO_2 substrate are destabilized by the thermocapillary forces at thicknesses larger than roughly 10 nm. For bilayers of Ag/Co on SiO_2/Si this threshold value is larger, possibly due to the reflectivity of the Si, which results in the distinctly different reflectivity curve of the system for small thicknesses.

Destabilization by thermocapillarity in thick Ag/Co films is manifested in the appearance of the secondary maximum on the linear dispersion curve at small wavenumbers. With the increase of h_{20}, this maximum grows fast and soon the associated wavelength prevails. We call this effect the *exchange of stability* (to not be confused with the principle of exchange of stabilities). Thus, this kind of destabilization leads to a larger spacing between particles upon dewetting. In Co/Ag films, the exchange of stability emerges in thin films (see Fig. 7), but the nature of the exchange is connected to the change of the energetics of the intermolecular forces as thickness changes and not to the thermocapillary destabilization. That is, thermocapillarity stabilizes thin Co/Ag films, just as it does stabilize thin Ag/Co films, as has been discussed.

C. Parameters

The typical values of the physical parameters for the Ag/Co/SiO_2/Si and Co/Ag/SiO_2/Si systems are shown in Table I. To the best of our knowledge, the *magnitudes* of the

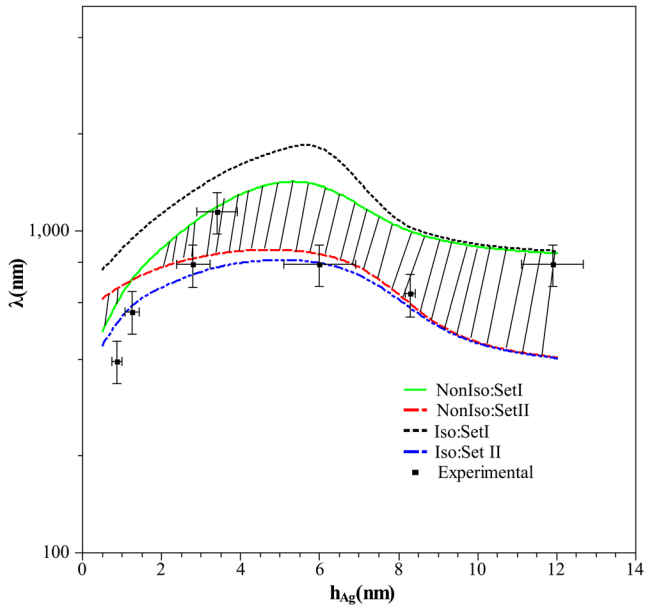

FIG. 6. (Color online) Particle spacing vs. the thickness of the top layer, for Ag/Co/SiO_2/Si system with the Co layer thickness fixed at 5 nm. Closed squares correspond to the experimentally determined particle spacings.[11] The solid (green) and dashed (red) lines enclosing the striped region correspond to the non-isothermal calculations, with the solid line corresponding to coefficient set I, and dashed line corresponding to coefficient set II (Table II). The short-dash (black) and dash-dotted (blue) lines correspond to the isothermal calculations with the top line for set I and bottom for set II.

Hamaker coefficients for the metallic systems like Ag/Co/SiO_2/Si or Co/Ag/SiO_2/Si are not known with precision and vary based on the type of calculation used to evaluate them, as noted in Ref. 11. Generally, values of the Hamaker coefficients may vary from 10^{-22} J to 10^{-18} J.[49,50] The choice of values of the Hamaker coefficients is very important, as has been emphasized in the published studies of thin bilayer systems.[33–35] Here, we have utilized the two sets of coefficients used in Ref. 11 which successfully bounded the experimental values based on the energy rate theory. The sets are shown in the Tables II and III. Note that the positive sign of a coefficient corresponds to destabilizing (attractive) interaction between interfaces.

It must be noted here that bilayer dynamics is very rich even in the isothermal case and can exhibit a large variety of evolution modes and outcomes, as was first noted by Pototsky *et al.*[32] Bandyopadhyay *et al.*[34] built a classification scheme of all possible evolution modes for the general isothermal polymer bilayer system, based on the extensive linear stability analysis supported by some nonlinear simulations. Our work extends this existing bilayer work by incorporating thermocapillary effects in the linear and nonlinear analysis for metallic liquids. For purposes of comparison, the two bilayer systems we have investigated can be most closely compared to Bandopadhyay *et al.* work via the surface energy classification scheme they have used. For example, the Co/Ag/SiO_2/Si system investigated here is similar to the case 3 in Bandopadhyay *et al.* as the surface energies of the substrate/gas interface ($\sigma_{sg} = 0.025$ J/m^2), liquid$_1$ (Ag)/gas interface ($\sigma_{1g} = 0.925$ J/m^2), and liquid$_2$ (Co)/gas interface ($\sigma_{2g} = 1.88$ J/m^2) are related as $\sigma_{sg} < \sigma_{1g} < \sigma_{2g}$,

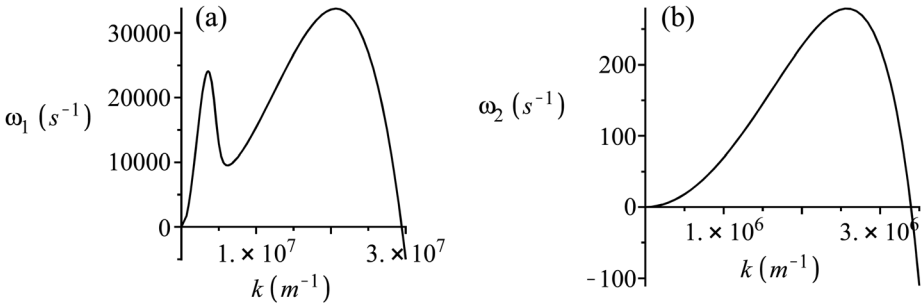

FIG. 7. Typical positive dispersion curves for the Co/Ag/SiO_2/Si system. Both ω_1 and ω_2 occur simultaneously as the solutions of Eq. (27).

while the Ag/Co/SiO_2/Si system is similar to their case 4, since $\sigma_{sg} < \sigma_{2g} < \sigma_{1g}$.

For convenience and ease of comparison with the results of the experiments we keep equations in the dimensional form. Another reason for working with the dimensional equations is that it is simply difficult to find convenient scales for the non-isothermal bilayer system (see Refs. 33, 35, 39, and 43) and, no matter how the scales are chosen, due to the large number of physical parameters, the number of dimensionless parameters will still be very large. In this paper, since the material system is fixed from the outset, we study the impacts of four parameters only: the upper layer thickness $h_{20} - h_{10}$ (where h_{10} is fixed) and the two sets of Hamaker coefficients.

III. LINEAR STABILITY ANALYSIS

Problems (1)–(14), (21), and (22) have a trivial, uniform equilibrium solution $h_1(x) = h_{10}$, $h_2(x) = h_{20}$. We introduce small perturbations $\xi_1(x,t) = U(t)\exp(ikx)$, $\xi_2(x,t) = V(t)\exp(ikx)$ (where k is the wavenumber and $U(t)$, $V(t)$ are the time-dependent small amplitudes) through $h_{1,2}(x,t) = h_{10,20} + \xi_{1,2}(x,t)$, and substitute the latter forms into the system (1)–(14), (21), and (22). Linearizing in $U(t)$, $V(t)$ gives the linear system of ordinary differential equations (ODE)

$$\dot{U}(t) = a_{11}U(t) + a_{12}V(t), \tag{23}$$

$$\dot{V}(t) = a_{21}U(t) + a_{22}V(t), \tag{24}$$

where the coefficients a_{ij} are the complicated functions (determined again with the help of the CAS) of k,$h_{10,20}$, the Hamaker coefficients, and other physical parameters. Next, substitution of $U(t) = u\exp(\omega t)$, $V(t) = v\exp(\omega t)$ into the system (23) and (24) results in the linear, homogeneous algebraic system for u and v

$$(a_{11} - \omega)u + a_{12}v = 0, \tag{25}$$

$$a_{21}u + (a_{22} - \omega)v = 0. \tag{26}$$

The condition for existence of a non-trivial solution to this system is the zero value of the determinant, which translates into the quadratic equation for the linear growth rate ω

$$\omega^2 - (a_{11} + a_{22})\omega + a_{11}a_{22} - a_{12}a_{21} = 0. \tag{27}$$

The latter equation may have two real and distinct solutions, one real solution, or two complex conjugate solutions. For the parameters of interest in this paper, only the first situation was ever found. In other words, only the monotonous modes of instability were detected.

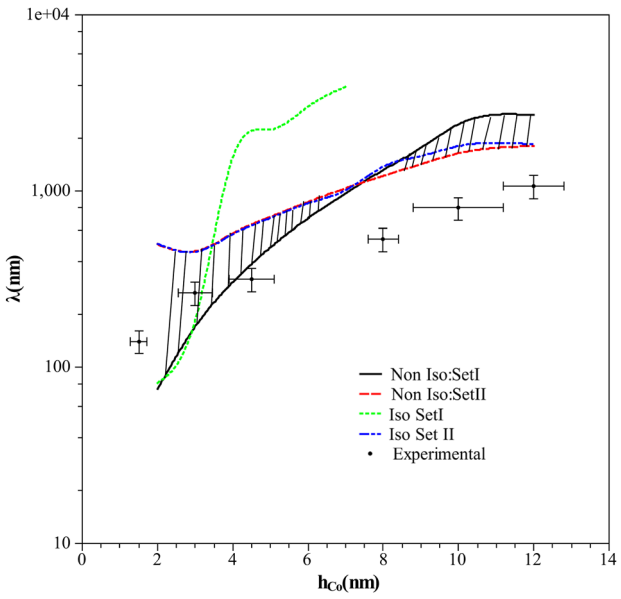

FIG. 8. (Color online) Particle spacing vs. the thickness of the top layer, for Co/Ag/SiO_2/Si system with the Ag layer thickness fixed at 5 nm. Closed squares correspond to the experimentally determined particle spacings.[11] The solid (black) and dashed (red) lines enclosing the striped region correspond to the non-isothermal calculations, with the solid line corresponding to coefficient set I, and dashed line corresponding to coefficient set II (Table II). The short-dash (green) and dash-dotted (blue) lines correspond to the isothermal calculations with the top line for set I and bottom for set II.

A. Ag/Co/SiO_2/Si system

For the Ag/Co/SiO_2/Si system, one solution of Eq. (27), $\omega_1(k)$, changes sign at a certain (single) value of k and the second solution, $\omega_2(k)$, is negative for all k. The typical dependence of ω_1 on k is shown in Fig. 5. Such dependence, characterized by a single maximum, is typical of long-wave instabilities. The value of k which corresponds to the maximum point on the $\omega_1(k)$ curve is the most dangerous (or critical) wavenumber of instability. The corresponding wavelength, $\lambda = 2\pi/k_{max}$, can be observed in the experiment: it has been shown that λ is a quite accurate measure of the particle spacing in the dewetting experiments on thin metal films.[17]

The theory predictions of the particle spacings vs. the thickness of the top (Ag) layer are shown in Fig. 6 for

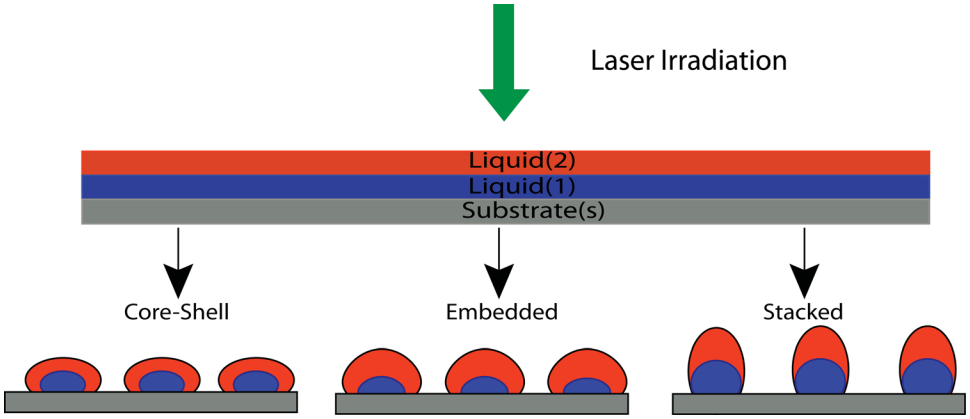

FIG. 9. (Color online). Sketch of the different self-organized nanostructure morphologies that can result from bilayer dewetting.

the two sets of the Hamaker coefficients, and compared to the experimentally determined particle spacings (closed squares). The experimentally determined values were taken from Ref. 11. The bottom layer (Co) thickness was kept constant at 5 nm. In this figure, the non-isothermal and isothermal predictions for each set of coefficients is shown. For the isothermal calculation, the temperature has been fixed at 1768 K (the melting temperature of Co) and the values of the surface tensions are equal to $\sigma_{1,2}^{(m)}$ (Table I). The upper and lower range of predictions of the non-isothermal pair are emphasized by the striped pattern. It can be seen that the non-isothermal calculation is a better overall predictor of the experimental data as compared to the isothermal case. In the simulations to be presented in Sec. IV, we compare results from both sets of coefficients, because together they provide a better overall prediction over the entire range of film thickness studied.

In Ref. 34, the following criterion is suggested for the determination of the deformation mode type in the linear (small interface deformation) regime: if the ratio

$$Q_L = \frac{\omega_{max} - a_{11}(k_{max})}{a_{12}(k_{max})}, \tag{28}$$

is positive [see Eqs. (25) and (26)], then the deformation mode is bending, otherwise it is squeezing (see Fig. 1). We applied this criterion to the Ag/Co/SiO_2/Si system *under isothermal and non-isothermal conditions*, and obtained the bending mode. This agrees fully with Ref. 34.

B. Co/Ag/SiO_2/Si system

For the Co/Ag/SiO_2/Si system, both solutions of Eq. (27) can change a sign at a certain (single) value of k (two-mode instability). However, the magnitude of the second solution, $\omega_2(k)$, is much less than the magnitude of the first solution, and thus the critical wavelength is still determined by the first solution. The typical dependencies of ω_1 and ω_2 on k are shown in Fig. 7. Note that the graph of ω_1 has both the relative and the absolute maxima; the critical wavenumber is one that corresponds to the absolute maximum. As the thickness of the top layer increases, the critical wavenumber approaches zero fast (thus λ increases), the more so if the exchange of stability occurs, in which case the critical wavenumber experiences a jump. For the upper layer thickness larger than 11 nm, both solutions become negative. Thus, thick bilayers are linearly stable.

The graphs of the particle spacings vs. the thickness of the top (Co) layer are shown in Fig. 8 for the two sets of the Hamaker coefficients, and compared to the experimentally determined particle spacings (closed squares). The bottom layer (Ag) thickness was kept constant at 5 nm. As in Fig. 6, the non-isothermal and isothermal predictions for the two sets are shown, with the non-isothermal case emphasized by

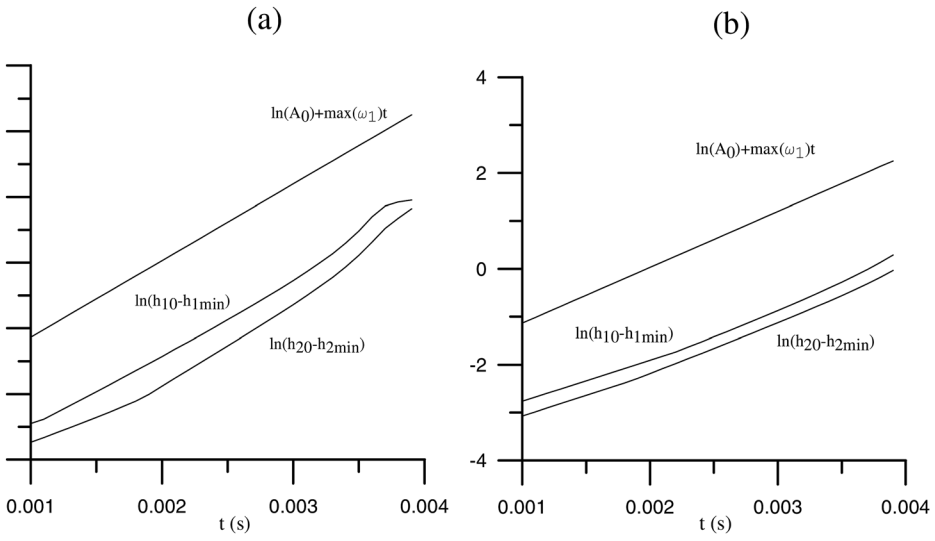

FIG. 10. Comparison of the computed growth rate of instability to the one predicted by the linear theory (Ag/Co, coefficient set I, see Fig. 11(b) for the film profiles). (a) Spatial grid resolution is 200 points; (b) 400 points. h_{1min} and h_{2min} are the minimum thicknesses of the layers over the computational domain.

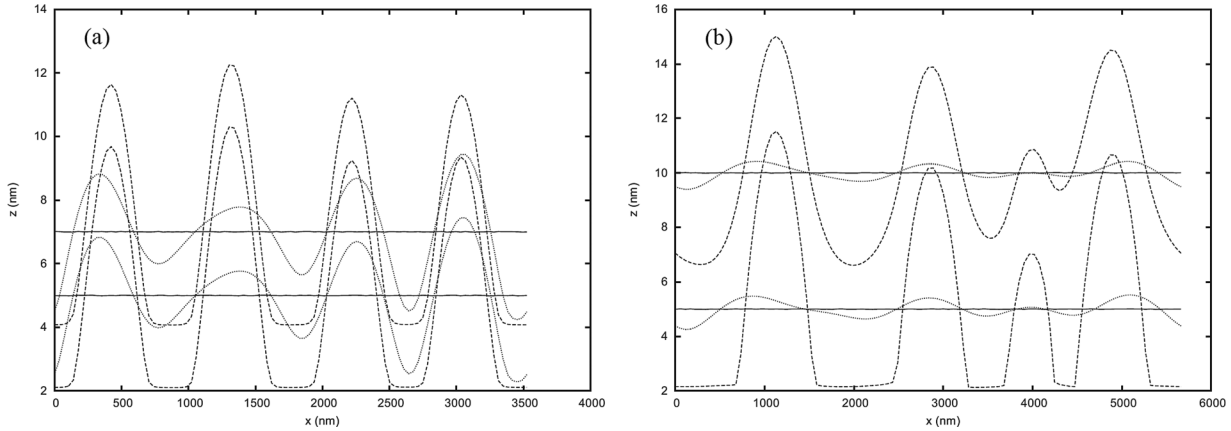

FIG. 11. Film profiles (core-shell morphology; Ag/Co, coefficient set I). (a) $h_{Co} = 5$ nm, $h_{Ag} = 2$ nm at $t = 0$ (solid line). Dotted line: $t = 1.39 \times 10^{-3}$ s; dashed line: $t = 2.49 \times 10^{-3}$ s. (b) $h_{Co} = 5$ nm, $h_{Ag} = 5$ nm at $t = 0$ (solid line). Dotted line: $t = 4.9 \times 10^{-3}$ s; dashed line: $t = 7.4 \times 10^{-3}$ s.

the striped pattern. Again, it can be seen that the non-isothermal calculation is a better overall predictor of the experimental data. One feature seen with the first set of the Hamaker coefficients (the isothermal case) is the abrupt jump in λ from 184 nm to 1550 nm when h_{Co} changes from 3 nm to 4 nm. This is due to the exchange of stability, signaling nearly the ten-fold decrease of the critical wavenumber. On the other hand, in the non-isothermal case, the second maximum is always larger than the first one and no such abrupt growth of the wavelength occurs. Similar jump in λ, but of much smaller magnitude, occurs in the isothermal case also for the second set of the Hamaker coefficients.

The application of the criterion (28) to the isothermal and non-isothermal Co/Ag/SiO_2/Si system indicates the squeezing mode of evolution (*in the linear regime*) for the first set of the Hamaker coefficients, and the bending mode for the second set.

IV. COMPUTATIONS OF THE BILAYER DEWETTING AND MORPHOLOGY EVOLUTION

Evolution Eqs. (1) and (2) were solved numerically using the method of lines. Integration in time is performed using the stiff ODE solvers RADAU or DVODE, whereas the discretization in space is carried out in the conservative form using the second order finite differencing on a spatially uniform grid. Below, we describe the results of the computations in the non-isothermal regime and compare, where appropriate, to the corresponding "isothermal" results. Dynamics of both systems was computed with the two sets of the Hamaker coefficients that are shown in the Tables II and III. For the Ag/Co/SiO_2/Si system, the outcomes are very similar, thus in Sec. IV A, we present the results only for the first set of coefficients. For the Co/Ag/SiO_2/Si system the outcomes are quite different, thus, we discuss the results for both sets of coefficients. Each run tracks the evolution of the most dangerous mode, λ, from the linear stability analysis. The length L of the computational domain in the x-direction equals 4λ. Periodic boundary conditions are imposed at $x = 0$ and $x = L$. The initial condition is small, uncorrelated, volume-preserving random perturbations of the mean thicknesses $h_{10,20}$ of the layers. To avoid films rupture at the substrate and to get insight into the dynamics of coarsening, the spreading coefficients were set to non-zero negative values $S_1 = -0.9\,\mathrm{J/m^2}$, $S_2 = -0.3\,\mathrm{J/m^2}$ (unless noted otherwise); the cut-off lengths are $\ell_{1,2} = 0.2$ nm. During each run, we also monitor the integral measure suggested by Pototsky *et al.*[33]

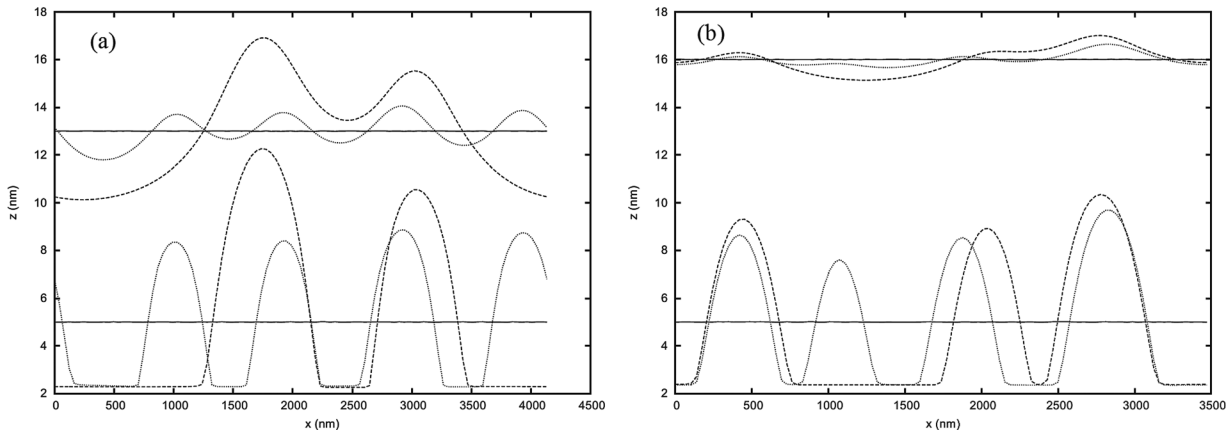

FIG. 12. Film profiles (embedded morphology; Ag/Co, coefficient set I). (a) $h_{Co} = 5$ nm, $h_{Ag} = 8$ nm at $t = 0$ (solid line). Dotted line: $t = 5.9 \times 10^{-3}$ s; dashed line: $t = 2.99 \times 10^{-2}$ s. (b) $h_{Co} = 5$ nm, $h_{Ag} = 11$ nm at $t = 0$ (solid line). Dotted line: $t = 8.9 \times 10^{-3}$ s; dashed line: $t = 3.11 \times 10^{-2}$ s.

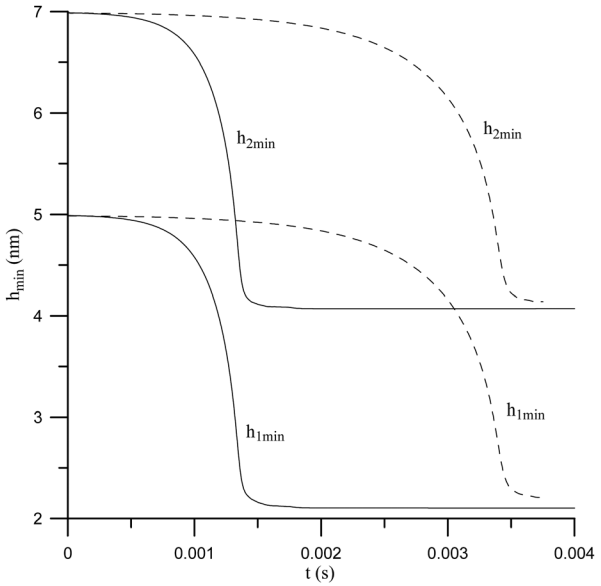

FIG. 13. Minimum total bilayer thickness h_{2min} and bottom layer thickness h_{1min} vs. time (Ag/Co, coefficient set I). Solid lines: non-isothermal evolution, dashed lines: isothermal one. $h_{Co} = 5$ nm, $h_{Ag} = 2$ nm at $t = 0$.

$$Q_{NL} = \frac{1}{L}\int \frac{(h_1 - h_{10})(h_2 - h_{20})}{\left[(h_1 - h_{10})^2 + (h_2 - h_{20})^2\right]} dx. \qquad (29)$$

Positive (negative) values of Q_{NL} signal the occurrence of the bending (squeezing) mode. Unlike the criterion (28), the measure (29) is applicable to nonlinear stages of the system evolution.

In all numerical experiments, the initial bottom layer thickness h_{10} is always 5 nm and the initial top layer thickness $h_{20} - h_{10}$ is varied (2 nm, 5 nm, 8 nm, and 11 nm for Ag/Co/SiO_2/Si system and 2 nm, 5 nm, and 7 nm for Co/Ag/SiO_2/Si system). Evolution in the non-isothermal systems is computed unless stated otherwise in the figure caption. As we discuss in the following sections, the final nanoparticle morphology can be classified as core-shell, embedded, and stacked structures, as shown in Fig. 9. We loosely define the core-shell morphology as one, where the maximum deformations of the liquid/gas and liquid/liquid interfaces at the end of the run do not differ by more than 20%, and the embedded morphology as one, where this difference is larger. In both cases, the top layer of liquid has to "coat" the bottom layer, in other words, the bottom layer is not exposed to the ambient gas. Stacked morphology can be defined as the limit of core-shell morphology as the thickness of the coating layer tends to zero.

In order to check the code, we compared the instability growth rate from the computations in the early stages of the evolution, when the interfacial deformations are small, with the growth rate from the linear stability theory. Fig. 10 shows the comparison for the Ag/Co/SiO_2/Si system and for two grid resolutions. Initially, interfaces are perturbed by a small random perturbation with the maximum amplitude $A_0 = 0.1$ nm. It can be seen in Fig. 10 that after very short initial transient when the random perturbation somewhat coarsens (not shown), the slopes of the numerical curves for both interfaces become very close to the slope ($= \max(\omega_1)$, see Fig. 5) of the straight line (linear theory), and the match improves on finer grid. At later times, i.e., at larger interfacial deformations when the system enters the nonlinear regime, the numerical slopes start to deviate from the linear theory.

All film profiles were computed with increasing resolution until convergence to within 5%; this usually requires 300–500 grid points–which is at the limit of our computing power, since resolving the temperature profile is very computationally intensive.

A. Ag/Co/SiO_2/Si system

As can be seen from Figs. 11 and 12, the bilayer evolves in the bending mode for all times, and this is in agreement with the dynamics of polymer bilayer films in case 4 of Ref. 34 within the linear theory's criterion (28). Also Q_{NL} (Eq. 29) is positive at all times, except sometimes in the early stages of the evolution when the initial roughness starts to coarsen into the four-wavelength profile. After such profile is formed (which is, in fact, four core-shell particles–see Fig. 9), its amplitude increases until a wetting layer is formed through the repulsive interaction with the substrate. Then, the profile coarsens again until only one large

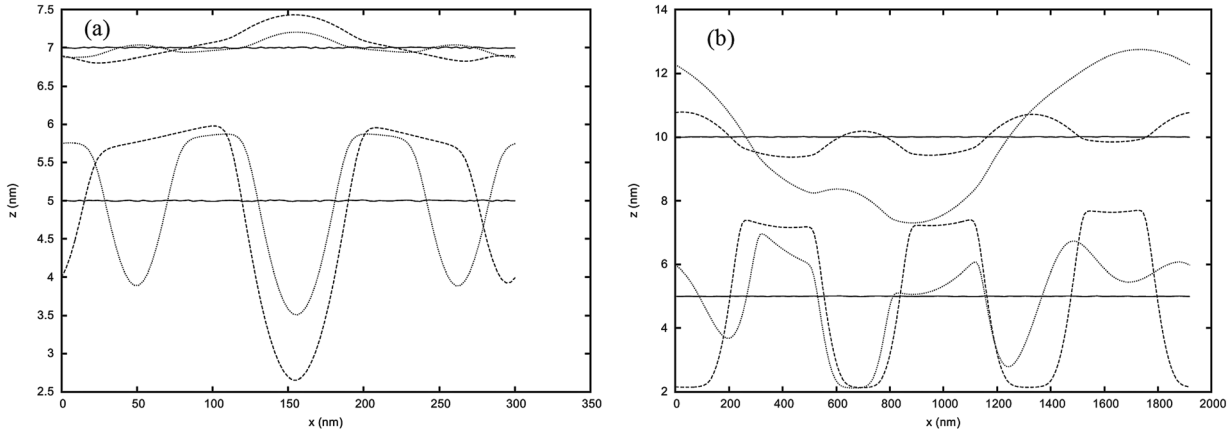

FIG. 14. Film profiles (embedded morphology; Co/Ag, coefficient set I). (a) $h_{Ag} = 5$ nm, $h_{Co} = 2$ nm at $t = 0$ (solid line). Dotted line: $t = 3.9 \times 10^{-6}$ s; dashed line: $t = 3.42 \times 10^{-5}$ s. (b) $h_{Ag} = 5$ nm, $h_{Co} = 5$ nm at $t = 0$ (solid line). Dotted line: $t = 9.9 \times 10^{-4}$ s; dashed line: $t = 3.4 \times 10^{-3}$ s.

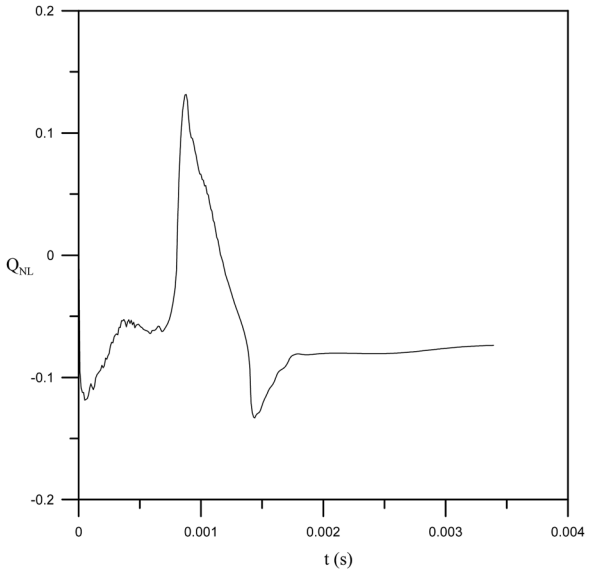

FIG. 15. Monitor function (29) for the evolution in Fig. 14(b).

core-shell particle remains. As an example, Fig. 12 show coarsening of the four-wavelength profile into a three- and two-wavelength profile. Note that in all cases, the time scale of the formation of the four-nanoparticle array is of the order of the total irradiation time in the experiments, given that one considers consecutive laser pulses without time delay (that is, 10 000 pulses × 10 ns (the duration of each pulse) = 10^{-4} s).

As these figures demonstrate, with the increase of the Ag thickness, the evolution of the Ag layer slows down significantly, resulting, for the sufficiently large Ag thickness, in the formation of Co particles embedded in the Ag matrix. The transition from core-shell particles to embedded ones occurs for Ag layer thickness between 6 and 8 nm.

The nonlinear evolution in the isothermal case does not differ significantly from the just described non-isothermal evolution. That is, the bilayer evolves in the bending mode at all times and core-shell particles form for the Ag layer thickness less than 6–8 nm, while embedded Co particles form for the larger Ag layer thickness. Of course, in accord with the linear stability analysis, see Fig. 6, the particle spacing (before coarsening occurs) is larger than in the non-isothermal case. Isothermal evolution is much slower than the non-isothermal one (Fig. 13) due to a capillary effect, i.e., the larger surface tensions ($\sigma_{1,2}^{(m)}$) compared to the non-isothermal one, Eqs. (11) and (12). This is generic for all nonlinear examples in this paper.

B. Co/Ag/SiO_2/Si system

For the first set of the Hamaker coefficients, the solution starts in the squeezing mode as predicted by Eq. (28), and then either continues in this mode for a thin Co film, or passes through the several periods of bending before settling in the squeezing mode for the thicker Co film. Fig. 14 shows the film profiles for $h_{Co} = 2$ nm and 5 nm. Fig. 15 shows the monitor function (29) for the latter case. It is clear from these figures that dewetting rate is significantly smaller than the rate of particle formation and coarsening, thus the Ag particles form on the surface of a thick Ag wetting layer, capped by the (almost planar) Co layer. The resulting morphology falls into "embedded" class.

Under isothermal conditions, the deformation mode is also squeezing for $h_{Co} = 2$ nm (and the morphology is similar to Fig. 14(a)), but for thicker Co film, it is bending. However, there is no particle formation in this latter case, since the Co layer dewets much faster than the Ag layer, and the bilayer ruptures when the Co/air interface reaches the Ag/Co interface. Such rupture can be prevented only by larger intermolecular repulsive forces between the interfaces; in this case, the rate of Co interface coarsening is much smaller than the rate of Ag interface coarsening, which results in multiple particles of Ag coexisting within the single particle of Co; this distinct embedded-type morphology is shown in Fig. 16(a). *When the interlayer repulsion is strong, same morphology occurs in the non-isothermal situation as well.* Note that in agreement with the analysis of Bandyopadhyay *et al.*,[34] no switching from bending to squeezing or vice versa occurs in the isothermal situation.

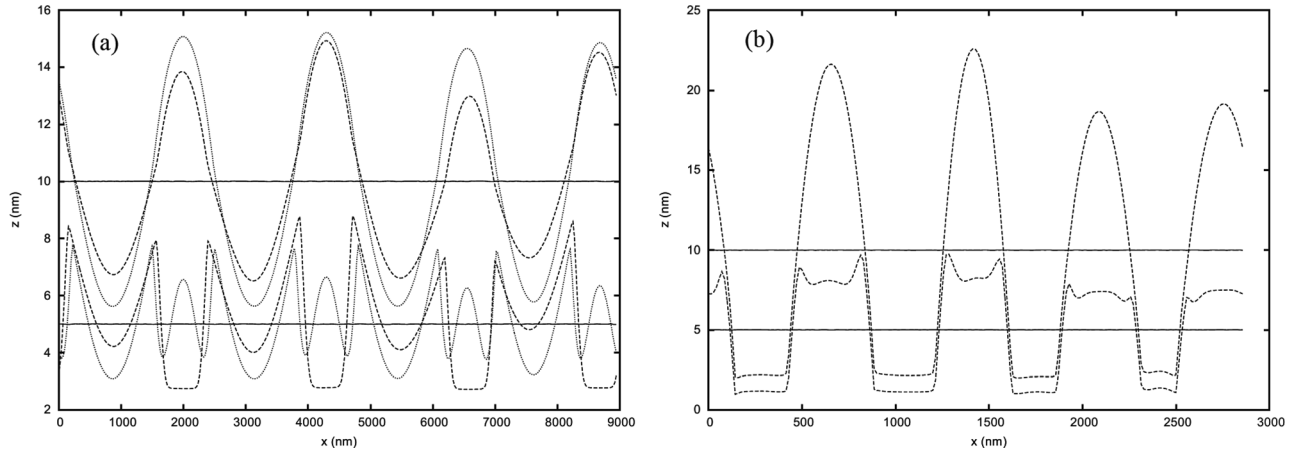

FIG. 16. Film profiles. (a) Core-shell morphology; Co/Ag, coefficient set I, isothermal, strong repulsion. $h_{Ag} = 5$ nm, $h_{Co} = 5$ nm at $t = 0$ (solid line). Dotted line: $t = 1.07 \times 10^{-3}$ s. Dashed line: $t = 4 \times 10^{-3}$ s. $S_1 = -14$ J/m^2, $S_2 = -40$ J/m^2. (b) Stacked morphology; Co/Ag, coefficient set II. $h_{Ag} = 5$ nm, $h_{Co} = 5$ nm at $t = 0$ (solid line). Dashed line: $t = 7.7 \times 10^{-6}$ s.

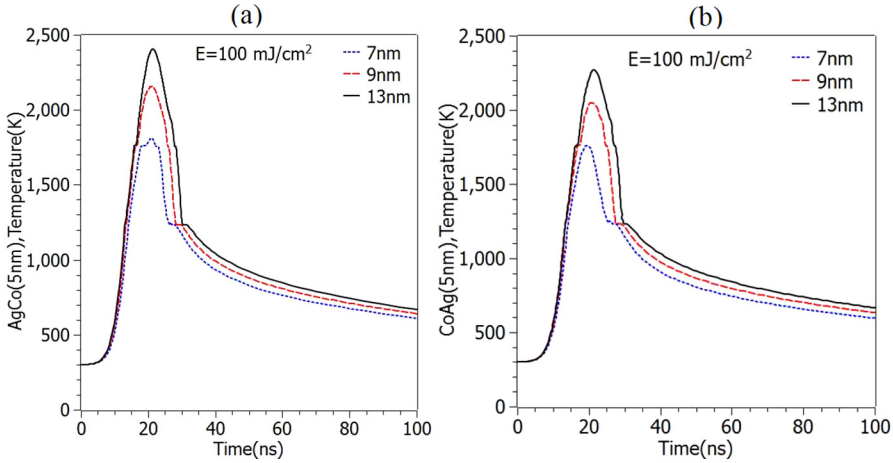

FIG. 17. (Color online) (a) Temperature of $Ag/Co/SiO_2/Si$ system vs. time. (b) Temperature of $Co/Ag/SiO_2/Si$ system vs. time. In this figure and in other figures in the Appendix, the key shows the total bilayer thickness, and the quantities plotted correspond to a single laser pulse.

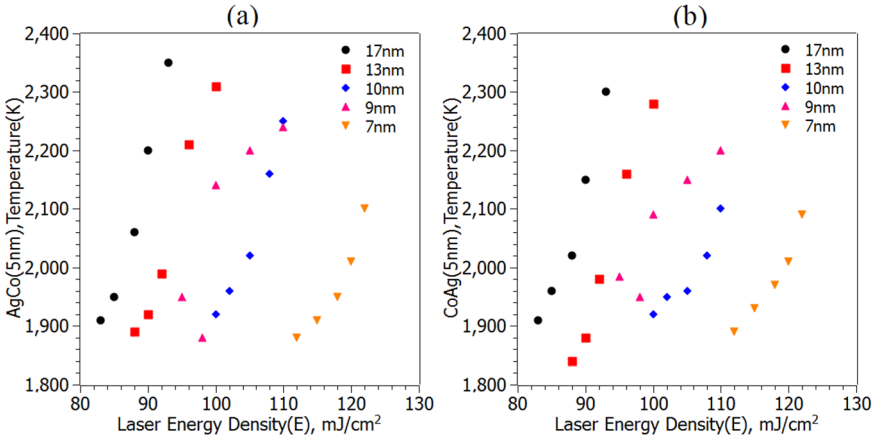

FIG. 18. (Color online) (a) Temperature of $Ag/Co/SiO_2/Si$ system vs. the laser energy density. (b) Temperature of $Co/Ag/SiO_2/Si$ system vs. the laser energy density.

For the second set of the Hamaker coefficients the evolution is entirely in the bending mode and is quite similar to the $Ag/Co/SiO_2/Si$ system. Fig. 16(b) shows one such morphology. By comparing to Fig. 11(b), one can notice that in the $Co/Ag/SiO_2/Si$ system, much smaller particles are formed from the bottom layer material and the shell (the top layer material) is thick at the top but very thin at the sides, while in the $Ag/Co/SiO_2/Si$ system, it is the opposite. In the real physical system, one expects point rupture (for instance, due to thermal fluctuations) of the Co layer at the side wall of the Ag particle, which results in the stacked morphology.

V. CONCLUSIONS

In this paper, the nanostructure-forming dynamics in pulsed-laser irradiated Ag/Co and Co/Ag thin bilayer films on an optically transparent substrate with a reflective support layer has been studied by means of a 2D linear stability analysis and nonlinear simulations. The long-wave approximation is employed. The full heat conduction problem, which includes the thickness dependent reflectivity and absorption in the bilayer is formulated, solved exactly, and the solution is coupled to the evolution equations for the thickness functions of the two layers. Intermolecular forces are accounted for in the evolution equations, and the thermocapillary (Marangoni) effect resulting from the thickness-dependent temperature is also taken into account at the gas-liquid and liquid-liquid interfaces. Linear stability analysis provides the nanoparticle spacing as a function of a thickness of a top layer. A better prediction of the experimental length scales was found for the non-isothermal calculations as compared to the isothermal case. This is a strong indication that thermocapillarity plays an important role in nanopatterning of laser-irradiated metallic bilayers. In the simulations, different pathways to core-shell, embedded and stacked nanoparticle morphologies were identified. These pathways are through the bending or squeezing evolution modes. The Ag/Co system evolved in the bending mode and core-shell nanoparticles form at the small-to-medium thicknesses of the top Ag layer; particles of Co embedded in the Ag matrix form at the large thicknesses of the Ag layer. The Co/Ag system may evolve in either a bending, or squeezing, or mixed mode, depending on the strengths of the intermolecular forces and the layers thicknesses. The squeezing and mixed modes lead to large embedded Ag particles. The bending mode most often leads to Co particles stacked on top of Ag particles. For the latter system, isothermal evolution and outcomes were distinctly different, which once again emphasized the critical importance of the thermocapillary effect.

ACKNOWLEDGMENTS

M. K. acknowledges the support of WKU Faculty Scholarship Council via Grant Nos. 10-7016 and 10-7054. R. K. acknowledges the support of NSF grants CAREER DMI-0449258 and CMMI-0855949. S. Y. and R. K. would also

like to thank Dr. Jeremy Strader for help with the bilayer optical reflectivity calculations.

APPENDIX: MODEL OF TRANSIENT HEATING BY THE GAUSSIAN LASER PULSE

The process of bilayer heating due to repetitive laser pulses of nanoseconds duration is described in 2D by

$$\rho C_p \frac{\partial T}{\partial t} = \nabla[k\nabla T] + Q_{laser}(y,t) + Q_m \frac{dy_i}{dt}. \quad \text{(A1)}$$

Here, the source terms account for laser heating and melting/freezing, C_p is the isobaric heat capacity, Q_m is the heat of melting of thin metal layers, and dy_i/dt is the rate of displacement of the solid/liquid interface located at y_i. (y is the axis normal to the planar, fixed surface pointing inward the material.)

$Q_{laser}(y,t)$, the laser heating contribution, is given by

$$Q_{laser}(y,t) = A(1-R(y))I(t)exp(-Ay), \quad \text{(A2)}$$

where $R(y)$ is the thickness dependent reflectivity and A is the absorption coefficient. Both the reflectivity and the absorption coefficients are calculated using the method described in Ref. 48. The incident laser power has Gaussian distribution,

$$I(t) = \sqrt{\frac{2}{\pi}}\frac{E}{\sigma}\exp\left(-\frac{2(t-\delta)^2}{\sigma^2}\right), \quad \text{(A3)}$$

where $\delta(18\,\text{ns})$ is the time at which the maximum intensity is reached, $\sigma(9\,\text{ns})$ is the width of the pulse, and E is the laser energy density in mJ/cm^2. For the system given by film$_1$/film$_2$/SiO$_2$/Si, the above heat equation was subject to the following boundary conditions:

(i) Sides are thermally insulated, and $T(y = h_{Si},t) = T_0$, where h_{Si} is the bottom of the substrate and $T_0 = 300\,\text{K}$;
(ii) $T(y,t = 0) = T_0$ at all interfaces;
(iii) At interior boundaries/interfaces, heat flow is taken as continuous ($k_{y1}\nabla T1 = k_{y2}\nabla T2$); and
(iv) Thermal radiation heat transfer at the top surface is neglected, as justified in Ref. 19.

The results were computed using the finite element software (FLEX-PDE). Figures 17 and 18 show the various quantities calculated.

[1]M. Zayats, S. Pogorelova, A. Kharitonov, O. Lioubashevski, E. Katz, and I. Willner, "An nanoparticle-enhanced surface plasmon resonance sensing of biocatalytic transformations," Chem.- Eur. J. **9**, 6108 (2003).
[2]R. Hirsch, E. Katz, and I. Willner, "Magneto-switchable bioelectrocatalysis," J. Am. Chem. Soc. **122**, 12053 (2000).
[3]M. Seydack, "Nanoparticle labels in immunosensing using optical detection methods," Biosens. Bioelectron. **20**, 2454 (2005).
[4]B. Sepulveda, A. Calle, L. M. Lechuga, and G. Armelles, "Highly sensitive detection of biomolecules with the magneto-optic surface-plasmon-resonance sensor," Opt. Lett. **31**, 1085 (2006).
[5]S. Tsunashima, "Magneto-optical recording," J. Phys. D: Appl. Phys. **34**, R87 (2001).
[6]S. Serrano-Guisan, G. Di Domenicantonio, M. Abid, J. P. Abid, M. Hillenkamp, L. Gravier, J. P. Ansermet, and C. Felix, "Enhanced magnetic field sensitivity of spin-dependent transport in clusterassembled metallic nanostructures," Nature Mater. **5**, 730 (2006).
[7]M. Abe and T. Suwa, "Surface plasma resonance and magneto-optical enhancement in composites containing multicore-shell structured nanoparticles," Phys. Rev. B **70**, 235103 (2004).
[8]K. Yang, C. Clavero, J. R. Skuza, M. Varela, and R. A. Lukaszew, "Surface plasmon resonance and magneto-optical enhancement on Au–Co nanocomposite thin films," J. Appl. Phys. **107**, 103924 (2010).
[9]J. B. Gonzalez-Diaz, A. Garcia-Martin, J. M. Garcia-Martin, A. Cebollada, G. Armelles, B. Sepulveda, Y. Alaverdyan, and M. Kall, "Plasmonic Au/Co/Au nanosandwiches with enhanced magneto-optical activity," Small **4**, 202 (2008).
[10]N. Pazos-Perez, Y. Gao, M. Hilgendorff, S. Irsen, J. Pereez-Juste, M. Spasova, M. Farle, L.M. Liz-Marzan, and M. Giersig, "Magnetic-noble metal nanocomposites with morphology-dependent optical response," Chem. Mater. **19**, 4415 (2007).
[11]H. Krishna, N. Shirato, S. Yadavali, R. Sachan, J. Strader, and R. Kalyanaraman, "Self-organization of nanoscale multilayer liquid metal films: Experiment and theory," ACS Nano **5**, 470 (2011).
[12]A. Vrij and J. Th. G. Overbeek, "Rupture of Thin Liquid Films Due to Spontaneous Fluctuations in Thickness," J. Am. Chem. Soc. **90**, 3074 (1968).
[13]G. Reiter, "Dewetting of thin polymer films," Phys. Rev. Lett. **68**, 75 (1992).
[14]A. Sharma and R. Khanna, "Pattern formation in unstable thin liquid films," Phys. Rev. Lett. **81**, 3463 (1998).
[15]R. M. Bradley and J. M. E. Harper, "Theory of ripple topography induced by ion bombardment," J. Vac. Sci. Technol. A **6**, 2390 (1988).
[16]E. Chason, T. M. Mayer, B. K. Kellerman, D. T. Mcllroy, and A. J. Howard, "Roughening instability and evolution of the Ge(001) surface during ion sputtering," Phys. Rev. Lett. **72**, 3040 (1994).
[17]J. Bischof, D. Scherer, S. Herminghaus, and P. Leiderer, "Dewetting modes of thin metallic films: Nucleation of holes and spinodal dewetting," Phys. Rev. Lett. **77**, 1536 (1996).
[18]S. J. Henley, J. D. Carey, and S. R. P. Silva, "Pulsed-laser-induced nanoscale island formation in thin metal-on-oxide films," Phys. Rev. B **72**, 195408 (2005).
[19]J. Trice, D. Thomas, C. Favazza, R. R. Sureshkumar, and R. Kalyanaraman, "Investigation of pulsed laser induced dewetting in nanoscopic metal films," Phys. Rev. B **75**, 235439 (2007).
[20]C. Zhang and R. Kalyanaraman, "In-situ nanostructured film formation during physical vapor deposition," Appl. Phys. Lett. **83**, 4827 (2003).
[21]C. Favazza, J. Trice, A. K. Gangopadhyay, H. Garcia, R. Sureshkumar, and R. Kalyanaraman, "Nanoparticle ordering by dewetting of Co on SiO2," J. Electron. Mater. **35**, 1618 (2006).
[22]J. Trice, C. Favazza, D. Thomas, H. Garcia, R. Kalyanaraman, and R. R. Sureshkumar, "Novel self-organization mechanism in ultrathin liquid films: Theory and experiment," Phys. Rev. Lett. **101**, 017802 (2008).
[23]H. Krishna, R. Sachan, J. Strader, C. Favazza, M. Khenner, and R. Kalyanaraman, "Thickness-dependent spontaneous dewetting morphology of ultrathin Ag films," Nanotechnology **21**, 155601 (2010).
[24]F. Brochard-Wyart, P. Martin, and C. Redon, "Liquid/liquid dewetting," Langmuir **9**, 3682 (1993).
[25]P. Lambooy, K. C. Phelan, O. Haugg, and G. Krausch, "Dewetting at the liquid-liquid interface," Phys. Rev. Lett. **76**, 1110 (1996).
[26]M. Sferrazza, M. Heppenstall-Butler, R. Cubitt, D. Bucknall, J. Webster, and R. A. L. Jones, "Interfacial instability driven by dispersive forces: The early stages of spinodal dewetting of a thin polymer film on a polymer substrate," Phys. Rev. Lett. **81**, 5173 (1998).
[27]M. O. David, G. Reiter, T. Sitthai, and J. Schultz, "Deformation of a glassy polymer film by long-range intermolecular forces," Langmuir **14**, 5667 (1998).
[28]R. A. Segalman and P. F. Green, "Dynamics of rims and the onset of spinodal dewetting at liquid/liquid interfaces," Macromolecules **32**, 801 (1999).
[29]C. Wang, G. Krausch, and M. Geoghegan, "Dewetting at a polymer-polymer interface: Film thickness dependence," Langmuir **17**, 6269 (2001).
[30]J. P. de Silva, M. Geoghegan, A. M. Higgins, G. Krausch, M. O. David, and G. Reiter, "Switching layer stability in a polymer bilayer by thickness variation," Phys. Rev. Lett. **98**, 267802 (2007).
[31]L. Xu, T. Shi, and L. An, "The competition between the liquid-liquid dewetting and the liquid-solid dewetting," J. Chem. Phys. **130**, 184903 (2009).
[32]A. Pototsky, M. Bestehorn, D. Merkt, and U. Thiele, "Alternative pathways of dewetting for a thin liquid two-layer film," Phys. Rev. E **70**, 025201 (2004).

[33]A. Pototsky, M. Bestehorn, and D. Merkt, "Morphology changes in the evolution of liquid two-layer films," J. Chem. Phys. **122**, 224711 (2005).
[34]D. Bandyopadhyay, R. Gulabani, and A. Sharma, "Instability and dynamics of thin liquid bilayers," Ind. Eng. Chem. Res. **44**, 1259 (2005).
[35]L. S. Fisher and A. A. Golovin, "Nonlinear stability analysis of a two-layer thin liquid film: Dewetting and authophobic behavior," J. Colloid Interface Sci. **291**, 515 (2005).
[36]D. Merkt, A. Pototsky, M. Bestehorn, and U. Thiele, "Long-wave theory of bounded two-layer films with a free liquid-liquid interface: Short- and long-time evolution," Phys. Fluids **17**, 064104 (2005).
[37]A. Pototsky, M. Bestehorn, D. Merkt, and U. Thiele, "Evolution of interface patterns of three-dimensional two-layer liquid films," Europhys. Lett. **74**, 665 (2006).
[38]D. Bandyopadhyay and A. Sharma, "Nonlinear instabilities and pathways of rupture in thin liquid bilayers," J. Chem. Phys **125**, 054711 (2006).
[39]A. A. Nepomnyashchy and I. B. Simanovskii, "Decomposition of a two-layer thin liquid film flowing under the action of Marangoni stresses," Phys. Fluids **18**, 112101 (2006).
[40]A. A. Nepomnyashchy and I. B. Simanovskii, "Marangoni instability in ultrathin two-layer films," Phys. Fluids **19**, 122103 (2007).
[41]A. A. Nepomnyashchy and I. B. Simanovskii, "The influence of gravity on the dynamics of non-isothermic ultra-thin two-layer films," Microgravity Sci. Technol. **21**, S261 (2009).
[42]H. Krishna, N. Shirato, C. Favazza, and R. Kalyanaraman, "Energy driven self-organization in nanoscale metallic liquid films," Phys. Chem. Chem. Phys. **11**, 8136 (2009).
[43]A. Atena and M. Khenner, "Thermocapillary effects in driven dewetting and self-assembly of pulsed-laser-irradiated metallic films," Phys. Rev. B **80**, 075402 (2009).
[44]C. Favazza, R. Kalyanaraman, and R. Sureshkumar, "Dynamics of ultra-thin metal films on amorphous substrates under fast thermal processing," J. Appl. Phys. **102**, 104308 (2007).
[45]S. H. Davis, "Thermocapillary instabilities," Annu. Rev. Fluid Mech. **19**, 403 (1987).
[46]A. Oron, S. H. Davis, and S. G. Bankoff, "Long scale evolution of thin liquid films," Rev. Mod. Phys. **69**, 931 (1997).
[47]R. V. Craster and O. K. Matar, "Dynamics and stability of thin liquid films," Rev. Mod. Phys. **81**, 1131 (2009).
[48]J. S. C. Prentice, "Coherent, partially coherent and incoherent light absorption in thin-film multilayer structures," J. Phys. D: Appl. Phys. **33**, 3139 (2000).
[49]V. M. Starov, M. G. Velarde, and C. J. Radke, *Wetting and Spreading Dynamics* (CRC, Boca Raton, 2007).
[50]J. Israelachvili, *Intermolecular and Surface Forces* (Academic, London, 1991).
[51]S. Yadavali and R. Kalyanaraman, "Thermal modeling for multilayer thin films using pulsed laser induced dewetting" (unpublished).